A Novel Adaptive Filtering-Based Tuning Loop for High-Q SRF Cavity

Yubing Shen,[1,2] Qiang Gu,[3] Xiang Zheng,[3] and Xuefang Huang[3]

[1]*Shanghai Institute of Applied Physics, Chinese Academy of Sciences, Shanghai 201800, China*
[2]*University of Chinese Academy of Sciences,Beijing 100049, China*
[3]*Shanghai Advanced Research Institute, Chinese Academy of Sciences, Shanghai 201210, China*

The Shanghai Hard X-ray Free Electron Laser (SHINE) facility utilizes high-Q 1.3GHz superconducting radio-frequency (SRF) cavities for particle acceleration. These cavities, with an ultra-narrow bandwidth of approximately 32 Hz, are highly susceptible to Lorentz force detuning (LFD) and microphonics, which can destabilize the cavity resonance frequency and compromise system performance. This paper presents a novel detuning compensation scheme that combines an autoregressive least-mean-square (LMS) adaptive filter and active noise control (ANC) in a parallel configuration to mitigate microphonic-induced detuning. A real-time simulation model, incorporating the cavity's mechanical eigenmodes, was developed to evaluate the proposed approach. Simulation results demonstrate significant reductions in amplitude and phase errors by approximately 90% and 75%, respectively, compared to the open-loop tuning configuration, achieving the stringent operational requirements. This study introduces an innovative detuning compensation strategy for high-Q SRF cavities, providing a robust framework for optimizing RF system design and ensuring stability in complex noise environments.

Keywords: Microphonics, RF cavity model, Tuning Loop

I. INTRODUCTION

SRF cavities are widely employed in modern particle accelerators [1][2][3]. Their high Q-factor design significantly reduces the operational costs of high-power systems but also introduces the risk of detuning due to their extremely narrow bandwidth [4][5]. Under high-load operating conditions, even minor frequency deviations can substantially impact the amplitude and phase stability within the cavity, leading to a significant increase in power demands [6][7][8]. In such scenarios, greater attention must be directed toward the tuning loop, requiring faster response times to compensate for detuning frequencies caused by external disturbances.

Cavity detuning primarily arises from two factors: LFD and microphonics. LFD, caused by the interaction between the electromagnetic field and wall currents, deforms the cavity and excites mechanical modes. However, when operating in continuous-wave (CW) mode, LFD can be effectively mitigated by pre-setting cavity detuning compensation in advance [9][10]. Microphonics, on the other hand, which has a significant impact in CW mode [11], includes deterministic disturbances such as those from cryogenic systems and vacuum pumps. These can be compensated using ANC, a method validated in facilities like LCLS-II [12]. For stochastic factors such as ground vibrations, adaptive filters are currently the most viable compensation approach. These detuning challenges demand fast response capabilities from the tuning loop. Taking SHINE as an example, the target is to maintain the RMS detuning frequency below 1.5 Hz [13]. Of course, there are also other methods, such as disturbance observer-based control (DOB) and iterative learning control (ILC) [14] [15], feedforward-based control [16], and active disturbance rejection control (ADRC) [17][18], among others.

To verify the effectiveness of various control measurements and algorithms in meeting the voltage stability requirements within the RF cavity, it is necessary to establish a real-time cavity simulation [19]. In addition to incorporating the cavity equivalent model and amplitude-phase feedback loops, it is crucial to develop a comprehensive and accurate tuning loop model. The tuning actuators responsible for compensating cavity detuning frequencies include stepper motor for slow tuning and piezo for fast tuning [20][21]. Both the piezo and the mechanical eigenmodes of the cavity are considered in the model. Using SHINE's accelerating cavities as an example, control parameters are ultimately adjusted to achieve an RMS voltage amplitude stability of less than 0.02% and an RMS phase stability of less than 0.02°.

The structure of this paper is as follows: It begins with a detailed discussion of the sources of detuning in high-Q RF cavities, focusing on the characteristics of microphonics and its impact on cavity stability. Sect. II evaluates various tuning loop control strategies and selects the LMS algorithm as the core for detuning compensation, analyzing potential instabilities in combination with system characteristics. Sect. III establishes a real-time simulation model incorporating the mechanical eigenmodes of the cavity to verify the effectiveness of different control strategies, with an in-depth analysis of the combined effects of ANC and LMS on suppressing amplitude and phase errors. Sect. IV concludes the paper.

II. CONTROL STRATEGY

A. Cavity Detuning Frequency and Changes in Control Strategies

In traditional normal conducting RF cavities or low-Q superconducting RF cavities, the tuning loop response frequency is typically designed to be relatively low to avoid coupling with the amplitude-phase loop [22]. For instance, the SSRF 500MHz superconducting cavity has a half-bandwidth of approximately 1.25 kHz. In such cases, detuning of a few Hz has minimal impact on the amplitude-phase stability of the

accelerating field inside the cavity. Therefore, a slow tuning loop with a response frequency of about 1-10 Hz is sufficient, while the amplitude-phase loop bandwidth generally ranges from 0.1-4 kHz [23].

In contrast, the SHINE main accelerating cavity has a resonance frequency of 1300 MHz and a loaded Q-factor as high as 4e7, resulting in a half-bandwidth of only about 16.25 Hz [24]. Under these conditions, detuning of just a few Hz can significantly degrade the amplitude-phase stability of the accelerating field, necessitating real-time compensation via fast tuning loop. However, simply increasing the tuning loop bandwidth may result in coupling with the amplitude-phase loop, and when the bandwidth reaches the scale of hundreds of Hz, it can even lead to system instability [25][26].

We conducted open-loop tests on the SHINE RF cavities, utilizing the widely adopted Schilcher cavity model based on state-space representation to inversely calculate the cavity detuning frequency [27][28][29]:

$$\begin{pmatrix} V'_{C,r(t)} \\ V'_{C,i(t)} \end{pmatrix} = \begin{pmatrix} -\omega_{1/2} & -\Delta\omega \\ \Delta\omega & -\omega_{1/2} \end{pmatrix} \begin{pmatrix} V_{C,r(t)} \\ V_{C,i(t)} \end{pmatrix} + \frac{2\beta}{\beta+1} \begin{pmatrix} \omega_{1/2} & 0 \\ 0 & \omega_{1/2} \end{pmatrix} \begin{pmatrix} V_{f,r(t)} \\ V_{f,i(t)} \end{pmatrix}, \tag{1}$$

V_C and V_f represent the cavity voltage and input voltage, respectively. The subscripts r and i indicate the real and imaginary components. $\omega_{1/2}$ represents the cavity half-bandwidth, $\Delta\omega$ is the cavity detuning angular frequency, and β is the coupling coefficient, which is typically much greater than 1 in high-Q loaded cavities. Under CW operation mode, the cavity detuning angular frequency at a steady state at time n can be expressed as:

$$\Delta\omega_{[n]} = \frac{2\beta}{\beta+1} \frac{\omega_{1/2}}{V^2_{C,r[n]} + V^2_{C,i[n]}} \left(V_{C,i[n]} V_{f,r[n]} - V_{C,r[n]} V_{f,i[n]} \right). \tag{2}$$

Under steady-state operating conditions, the time-domain and frequency-domain plots of cavity detuning frequency are shown in Fig. 1. Since the impact of LFD under steady-state CW operation is negligible [30], the detuning is primarily caused by microphonics. By analyzing the spectral plot of the detuning frequency, its primary characteristics can be identified. First, prominent spectral components are observed at DC and specific frequency points. Noise source testing indicates that these components are primarily caused by mechanical devices, such as cryogenic systems and helium pressure fluctuations, which generate significant detuning at these frequencies and their vicinities [31]. When these devices are turned off, the corresponding noise levels are significantly reduced. This suggests that optimizing noise sources to minimize mechanical vibrations is an effective mitigation strategy. Additionally, control algorithms targeting specific frequency points, such as ANC, can be employed to further suppress these noise components.

Second, the remaining spectral components are mainly distributed below 250 Hz, where scattered random noise dominates. This frequency range also coincides with the mechanical eigenmodes of the cavity. The next section will focus on the use of real-time adaptive filters to suppress noise within this frequency band.

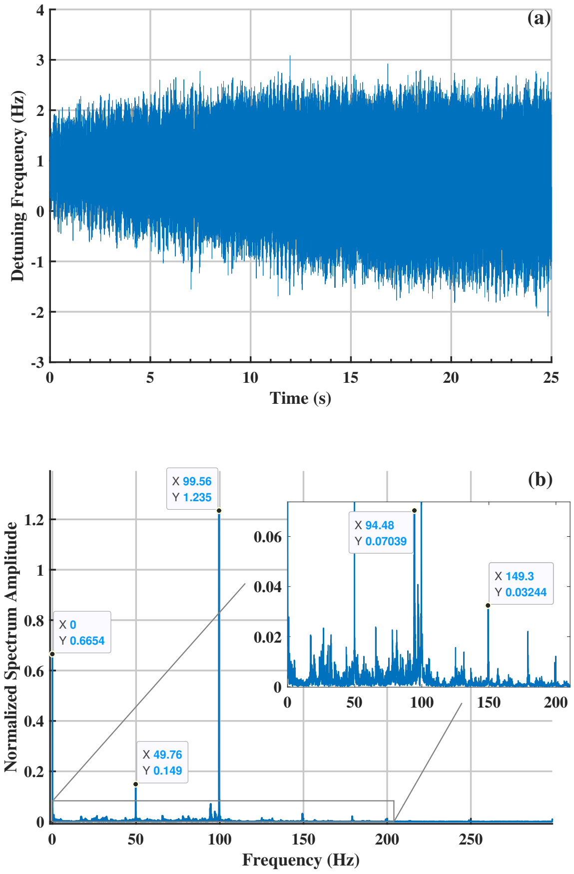

Fig. 1. (Color online) Time-Domain (a) and Frequency-Domain (b) Representations of the Cavity Detuning Frequency.

In summary, the proposed control logic block diagram is presented in Fig. 2.

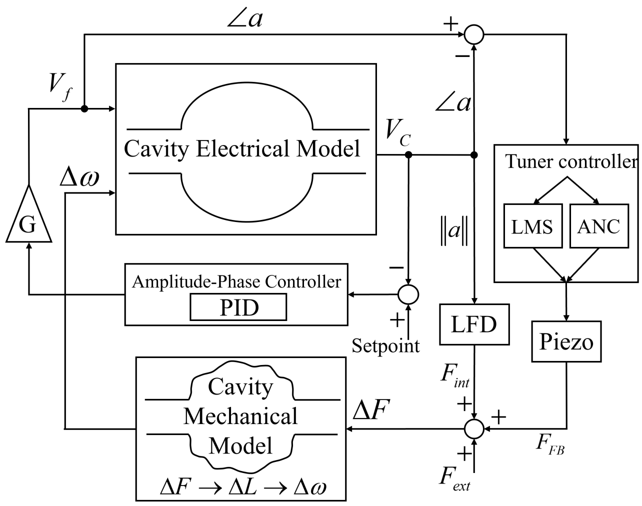

Fig. 2. Control Logic Block Diagram of the System Loop.

Here, $\|a\|$ denotes the magnitude, and $\angle a$ represents the phase angle. The amplitude-phase loop employs PID control,

while the tuning loop adopts a real-time adaptive filter combined with the ANC for better suppression of cavity detuning. Regardless of the source of noise, the process ultimately applies forces to the cavity, causing deformation and resulting in changes to the cavity's resonant frequency. This process is modeled in the Cavity Mechanical Model block, which will be discussed in greater detail in Sect. III. The Lorentz force generated by RF fields is referred to as F_{int}, while the force caused by microphonics is denoted as F_{ext}. The feedback loop applies a force through the piezo, which is labeled as F_{FB}.

B. Control Algorithm

An adaptive filter is a dynamic filter capable of automatically adjusting its parameters based on changes in the input signal. Its core functionality lies in minimizing the error signal through iterative algorithms, enabling effective signal extraction and noise suppression. Unlike traditional fixed-parameter filters, adaptive filters do not require pre-defined filtering parameters. Instead, they utilize algorithmic optimization techniques to dynamically update filter coefficients in real-time, allowing them to adapt to time-varying signal environments [32].

If cavity frequency detuning is considered as interference noise, suppressing this noise typically requires a reference noise signal that is correlated with the target noise to be suppressed. In the RF cavity operating environment, the reference noise signal can be selected as the previously suppressed noise from the last time step, implementing an uncommon autoregressive strategy.

To evaluate the effectiveness of this control strategy, this study uses a single-tone 20 Hz signal with a signal-to-noise ratio (SNR) of 30 as the test signal. The signal is subjected to autoregressive suppression using three different adaptive filtering methods: least-mean-square (LMS) adaptive filter, recursive least squares (RLS) filter, and Kalman adaptive filter.

$$\begin{cases} {}_{n} = [w_0(n), w_1(n), \cdots, w_{N-1}(n)]^T \\ x_n = [x(n), x(n-1), \cdots, x(n-N+1)]^T \\ x(n+1) = e(n) = d(n) - x_n^T \cdot w_n \end{cases}, \tag{3}$$

FIR filter w_n represents the filter coefficients at step n with a length of N, and x_n represents the reference noise signal with a depth of N. It can be observed that the filter output is composed of a step-by-step combination of noise suppressed in previous iterations.

$$w_{n+1} = w_n + \mu e_{(n)} x_n. \tag{4}$$

Eq. 4 represents the basic form of the LMS filter, where the only parameter requiring initial configuration is the learning rate μ.

$$\begin{cases} K_n = \dfrac{P_n x_n}{\lambda + x_n^T P_n x_n} \\ w_{n+1} = w_n + K_n e_{(n)} \\ P_{n+1} = \dfrac{1}{\lambda}\left(P_n - K_n x_n^T P_n\right) \end{cases}. \tag{5}$$

Eq. 5 represents the basic form of the RLS filter, where P_n denotes the covariance matrix at step n. If the initial P_0 is relatively large, the filter tends to be more conservative in the initial stages, with a slower learning rate. while smaller P_0 allows faster weight adjustments. The parameter λ is the forgetting factor, typically within the range of 0 to 1. When there is a higher reliance on historical data, λ should be closer to 1.

$$\begin{cases} P_{n|n-1} = P_{n-1|n-1} + Q \\ K_n = P_{n|n-1} x_n \left(x_n^T P_{n|n-1} x_n + R\right)^{-1} \\ w_{n+1} = w_n + K_n e_{(n)} \\ P_{n|n} = \left(I - K_n x_n^T\right) P_{n|n-1} \end{cases}. \tag{6}$$

Eq. 6 represents the basic form of the Kalman filter, where P_n is the covariance matrix at step n, Q is the process noise covariance matrix, and R is the observation noise covariance matrix. Increasing Q allows the filter to respond more quickly to changes in the signal, while increasing R reduces the influence of observation noise.

The test signal is subjected to autoregressive suppression using the three adaptive filters described above:

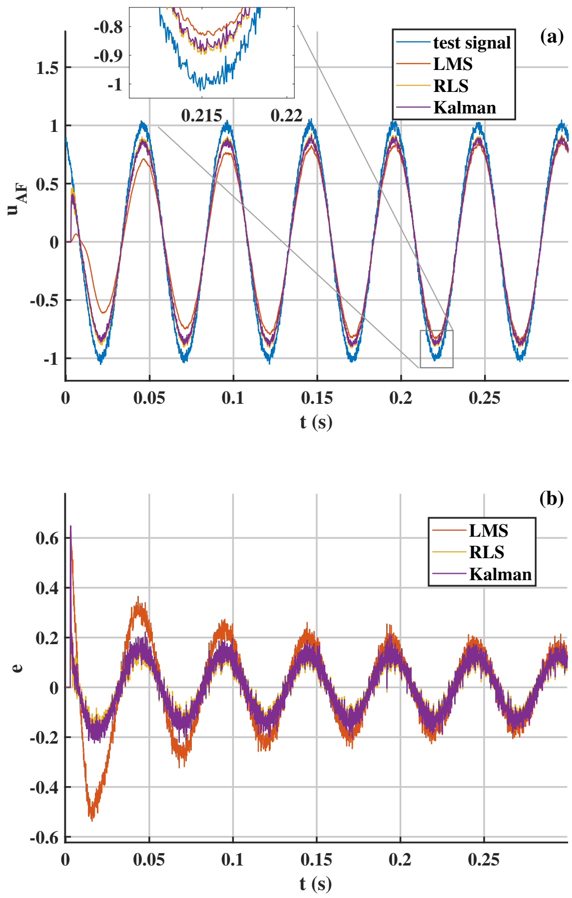

Fig. 3. (Color online) Outputs (a) and Errors (b) of Three Adaptive Filters Based on the Autoregressive Strategy.

As shown in Fig. 3, the LMS method reaches optimal suppression more slowly compared to RLS and Kalman filters. However, regardless of how the parameters of RLS and Kalman filters are adjusted, the final suppression effectiveness is nearly identical across all three methods. This conclusion is further supported by the FIR tap coefficients.

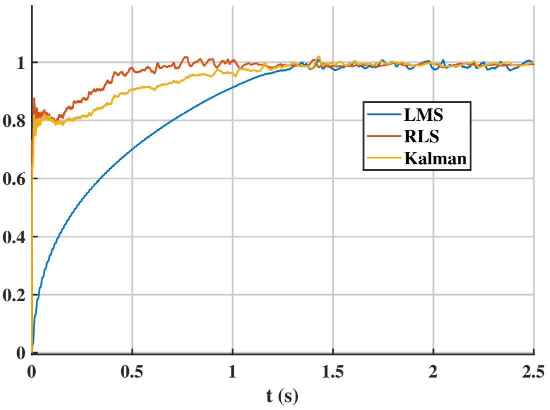

Fig. 4. (Color online) Comparison of the First Tap Coefficient of Three Adaptive Filters Based on the Autoregressive Strategy.

The tap coefficients eventually converge to the same value across all three methods. While RLS and Kalman filters can achieve rapid convergence in a short time, they involve matrix multiplications and inversions, which typically consume significant resources in FPGA implementations. Under these constraints, this study selects the LMS algorithm as the adaptive filter's core algorithm.

The above discussion focuses on using adaptive filters to suppress uncertain noise. In contrast, a 2019 solution proposed by Cornell University introduced an ANC approach for RF cavities [4], which effectively suppresses noise at fixed frequencies:

$$\begin{cases} u_{ANC(t)} = \sum\limits_{m} u_{m(t)} = \sum\limits_{m} I_{m(t)} \cos\left(\omega_m t\right) - Q_{m(t)} \sin\left(\omega_m t\right) \\ I_{m(n+1)} = I_{m(n)} - \gamma \cdot \delta f_{comp(n)} \cdot \cos\left(\omega_m t - \phi_{m(n)}\right) \\ Q_{m(n+1)} = Q_{m(n)} + \gamma \cdot \delta f_{comp(n)} \cdot \sin\left(\omega_m t - \phi_{m(n)}\right) \\ \phi_{m(n+1)} = \phi_{m(n)} - \eta \cdot \delta f_{comp(n)} \cdot \left[I_{m(n)} \sin\left(\omega_m t - \phi_{m(n)}\right) \right. \\ \qquad \left. + Q_{m(n)} \cos\left(\omega_m t - \phi_{m(n)}\right)\right] \end{cases} \tag{7}$$

The subscript m indicates that ANC suppression can be applied at different frequency points. γ and η are the learning rates for I_m/Q_m and ϕ_m, respectively. Here, the adaptation of ϕ_m is designed to compensate for the phase of the actuator at the corresponding frequency point. It is worth noting that when ϕ_m is nonzero, the closed-loop transfer function formed by ANC may exhibit loop gain greater than 1 at the set frequency. This results in the unintended amplification of noise at the surrounding frequencies, even though ANC significantly suppresses noise at the set frequency.

C. Potential Instabilities

Adaptive filters employing autoregressive strategies must pay particular attention to potential instability issues. These primarily arise due to the absence of an external reference signal, as filter coefficient adjustments rely on historical estimation data derived from the autoregressive process. This makes the performance heavily dependent on the dynamic changes in noise and the rate of filter tap coefficients update. Specifically, if the loop delay is too large, the autoregressive non-standard reference signal may exhibit weak correlation with the current external noise signal, leading to degraded filtering performance. Additionally, the rate of change of the filter tap coefficients must be carefully considered. If the rate is too small, the filter may struggle to accurately track and suppress noise. Conversely, if the rate is too large, it can result in self-excitation and instability.

Specific parameters that need to be configured include the order of the FIR filter N, the LMS update frequency f_{AF}, and the LMS learning rate μ. Using the cavity detuning data shown in Fig. 1 as the test noise, the following analysis focuses solely on the LMS single-loop configuration:

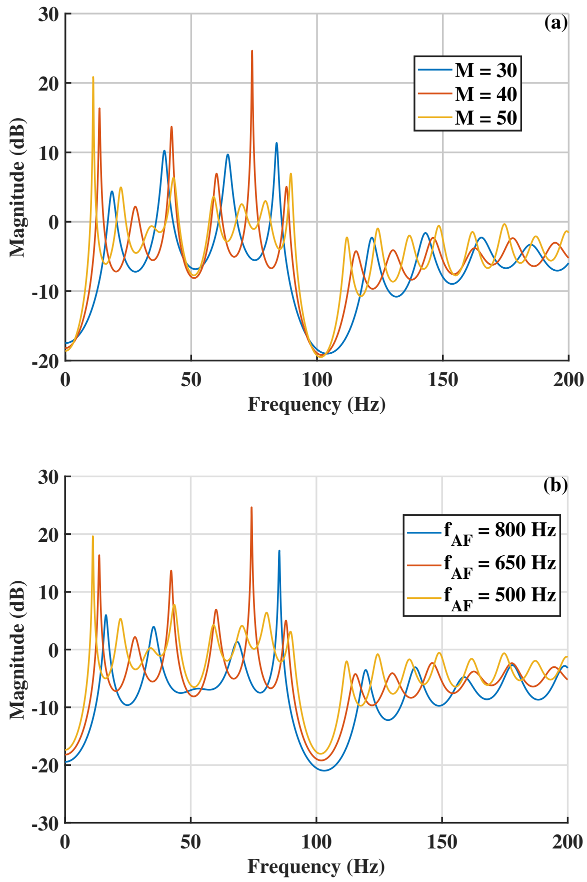

Fig. 5. (Color online) Closed-Loop Amplitude-Frequency Response Curves Under Different Filter Orders (a) and LMS Update Frequencies (b).

When the filter order is higher and the LMS update fre-

quency is lower, the filter achieves higher resolution within the specified frequency band, resulting in better noise suppression performance.

The NLMS algorithm is proposed to address the issue of uneven coefficient update rates caused by the LMS algorithm. By dynamically adjusting the learning rate based on the energy of the autoregressive signal, the convergence speed can be increased when the signal energy is low and decreased when the energy is high. The update equation for NLMS is as follows:

$$\begin{cases} w_{n+1} = w_n + \dfrac{\mu}{\|x_n\|^2 + C} e_{(n)} x_n \ . \end{cases} \tag{8}$$

Similarly, the cavity detuning data mentioned in Fig. 1 is used as the test noise for simulation testing:

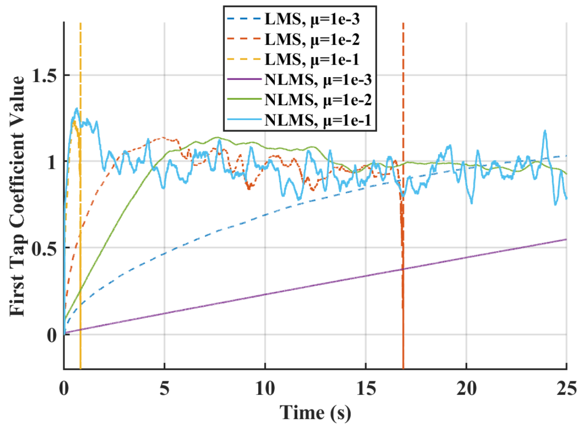

Fig. 6. (Color online) Comparison of the First Tap Coefficient of Three Adaptive Filters Based on the Autoregressive Strategy.

The learning rate μ in LMS has a narrower range of variability compared to NLMS, making it more prone to instability and causing divergence in the tap coefficients, as indicated by the dashed lines at 1s and 16s in the figure. Additionally, NLMS exhibits an almost linear progression before reaching stability.

From the above results, it can be observed that LMS has limited effectiveness in suppressing noise at specific frequency points within a certain timeframe. In such cases, ANC can compensate for the insufficient gain.

III. SIMULATION MODEL AND TEST RESULTS

A. Mechanical Eigenmodes of the Cavity

The mechanical characteristics of the cavity determine the extent to which external forces can couple to the eigenmodes of the nine-cell structure, potentially exciting unwanted oscillations. In piezo-based detuning control, it is crucial to measure the transfer function between the piezo drive signal and the cavity detuning [33]. The smoothed test results for the SHINE cavity are shown below:

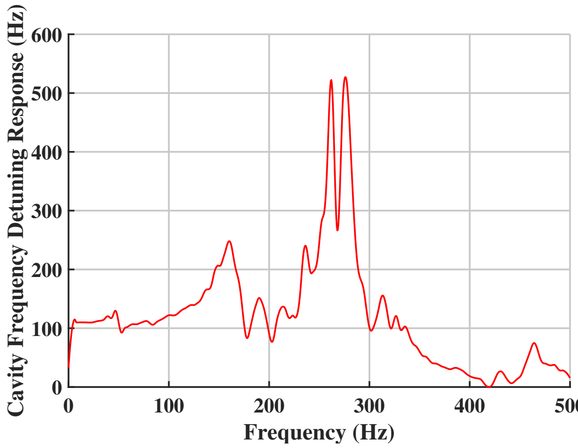

Fig. 7. (Color online) Cavity Frequency Detuning Response to Sine Wave Excitations of Different Frequencies on Piezo.

The response transfer function can be modeled using a first-order low-pass filter combined with several second-order systems [34]:

$$H_{(s)} = H_{0(s)} + \sum\nolimits_i H_{i(s)} = \frac{K_0}{\tau s + 1} + \sum\nolimits_i \frac{K_i \cdot \Omega_i^2}{s^2 + \frac{\Omega_i}{Q_i} s + \Omega_i^2}, \tag{9}$$

The second-order systems correspond to the mechanical eigenmodes of the cavity. What is observed in the control loop is the process that starts with the piezo drive signal, followed by the force applied to the tuner, resulting in cavity deformation, and ultimately causing a change in the cavity's resonant frequency. The cavity stiffness $k_S = 3 \times 10^6 N/m$, and the process is illustrated in Fig. 8.

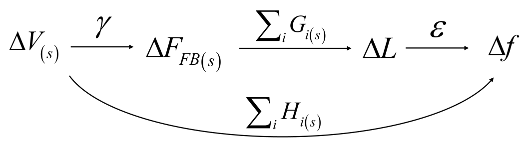

Fig. 8. Process Analysis from Piezo Drive Signal to Cavity Frequency Detuning.

In mechanical dynamics, cavity deformation can be decomposed into a set of mechanical modes. When a specific mode is excited, it produces the corresponding mode displacement. Since the applied forces remain within the cavity's linear elastic limit, these modes can be represented as a set of damped harmonic oscillators:

$$G_{i(s)} = \frac{k_i \cdot \Omega_i^2}{s^2 + \frac{\Omega_i}{Q_i} s + \Omega_i^2}. \tag{10}$$

Considering that the piezo response is relatively flat below 1 kHz, meaning that the force applied under the same voltage is nearly constant across different frequencies, and assuming that cavity deformation is linearly related to cavity frequency detuning ($\varepsilon \approx 3.4 \times 10^8 Hz/m$), from the Eq. 11:

$$\sum_{i=1}^{n} H_{(s)}|_{s=0} = \gamma \cdot \sum_{i=1}^{n} G_{(s)}|_{s=0} \cdot \varepsilon \rightarrow \sum\nolimits_i K_i = \gamma \cdot \varepsilon / k_S, \tag{11}$$

we can derive the gain γ, and further obtain the transfer function G with the modal gains k_i.

By using the least-squares method, it is possible to approximate the forces exerted on the cavity due to microphonics.

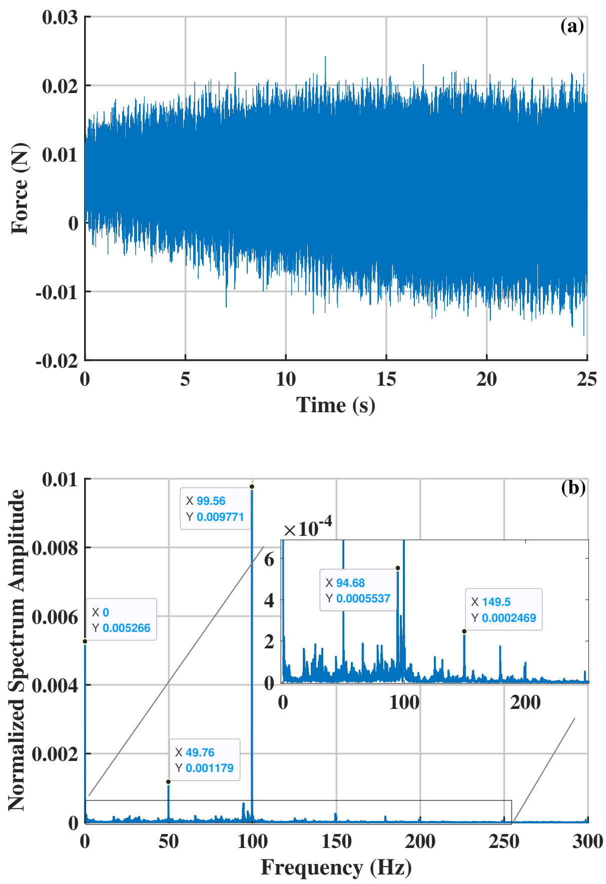

Fig. 9. (Color online) Time-Domain (a) and Spectrum Diagrams (b) of Force Applied by Microphonics on the Cavity.

Similarly, the effect of LFD can be expressed by Eq. 12:

$$F_{int} = \sum\nolimits_i F_{int,i} = \sum\nolimits_i \frac{k_{lfd}^i V_C^2}{k_i \varepsilon L^2}, \tag{12}$$

Here, k_{lfd}^i is the LFD constant [35], with units of $Hz/(MVm^{-1})^2$.

This concludes the introduction of the cavity mechanical modes and the forces applied to the cavity, as illustrated in Fig. 9.

B. Amplitude-Phase Loop and Tuning Loop in Closed-Loop Operation

During steady-state operation of the RF system, the LLRF operates in GDR mode. This study analyzes the impact of different tuning loop configurations on the amplitude and phase stability of the cavity voltage by experimentally observing various operating states of the tuning loop, including open-loop, closed-loop using only the LMS algorithm, and closed-loop with LMS and ANC in parallel.

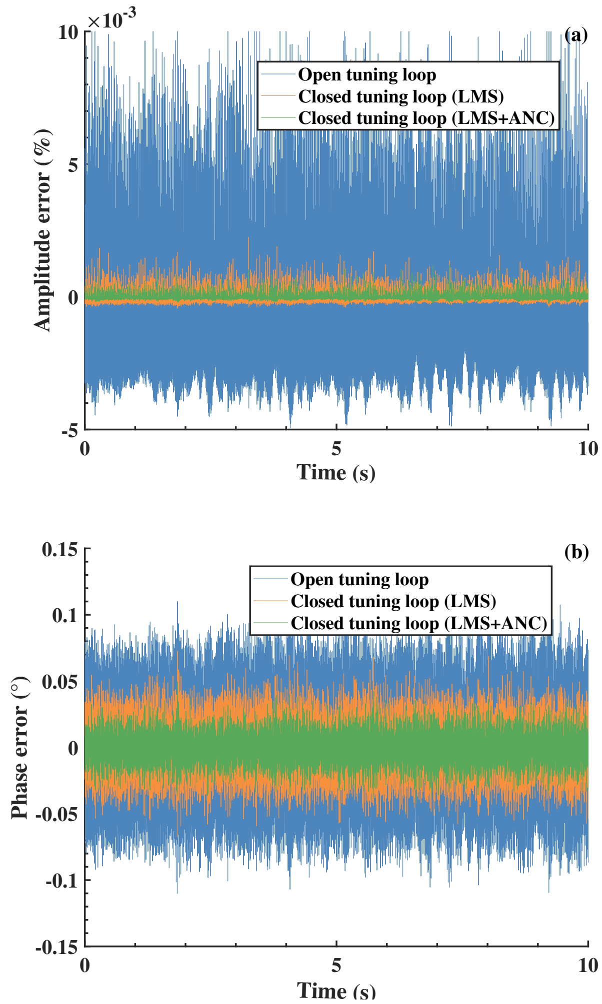

Fig. 10. (Color online) Amplitude (a) and Phase (b) Error Curves of the Cavity Under Three Conditions: Open Tuning Loop, Closed Loop with LMS, and Closed Loop with LMS+ANC.

As shown in Fig. 10, the amplitude and phase error curves over a 10-second interval under steady-state conditions were recorded and analyzed. The RMS values of amplitude error for the three configurations were 0.0031%, 0.0004%, and 0.0002%, respectively, while the RMS values of phase error were 0.0457°, 0.0176°, and 0.0113°, respectively. The data demonstrate that the amplitude stability significantly improves when the tuning loop is closed. Using only the LMS algorithm, the tuning loop effectively compensates for noise

disturbances, achieving basic amplitude and phase stability. However, with the addition of ANC, the system's ability to suppress noise at specific frequency points is significantly enhanced, resulting in the lowest RMS phase error.

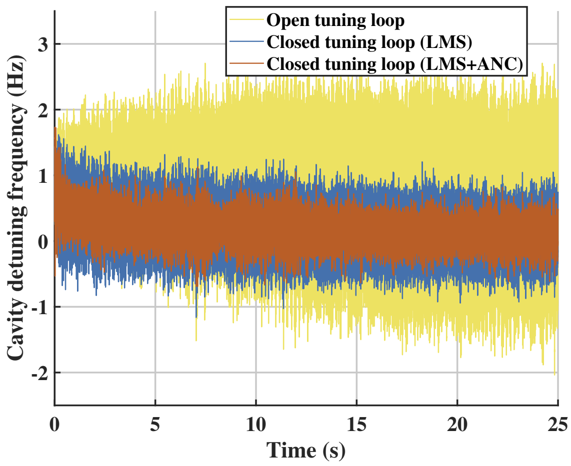

Fig. 11. Cavity Detuning Frequency Under Different Tuning Strategies.

Fig. 11 provides a clearer illustration of cavity detuning under different strategies. Since the ANC algorithm cannot fully compensate cavity detuning to the zero-detuning position and is limited to compensating for a few specific frequency points, both the LMS algorithm and the widely used PID control strategy in current tuning loop can effectively suppress cavity detuning to the zero-detuning position.

IV. CONCLUSION

This study addresses the high-precision operational requirements of the SHINE by proposing a detuning compensation scheme that significantly improves system amplitude and phase stability. Through an in-depth comparison of commonly used adaptive filtering algorithms, and considering both performance and hardware implementation costs, the autoregressive LMS algorithm was selected. Its parameter design and potential instabilities were analyzed, focusing on filter order, update frequency, and learning rate. Simulations demonstrated the algorithm's efficiency in suppressing uncertain noise.

To accurately simulate the operating environment of RF cavities, a simulation model incorporating the cavity's mechanical eigenmodes was established. Combined with amplitude-phase feedback and tuning loops, the performance of various control algorithms was analyzed in detail. Experimental and simulation results showed that the parallel scheme of the autoregressive LMS and ANC algorithm effectively suppressed microphonic detuning. Compared to the open-loop tuning configuration, the amplitude error and phase error were reduced by approximately 90% and 75%, respectively, meeting SHINE's operational requirements.

This study not only demonstrates the potential of adaptive filters in suppressing RF cavity detuning but also establishes a foundational framework for further tuning loop optimization through the construction of the cavity simulation model. Future work will focus on enhancing the robustness of the proposed scheme in dynamic environments, supporting the stable operation of the SHINE facility and providing insights for the design of high-precision particle accelerators.

[1] C. Xu, I. Ben-Zvi, HOM frequency control of SRF cavity in high current ERLs. Nucl. Instrum. Methods Phys. Res., Sect. A. **883**, 136–142 (2018). doi: 10.1016/j.nima.2017.11.074

[2] Y.X. Zhang, J.F. Chen, D. Wang, RF design optimization for the SHINE 3.9 GHz cavity. Nucl. Sci. Tech. **31**, 73 (2020). doi: 10.1007/s41365-020-00772-z

[3] J. Liu, H. Hou, D. Mao et al., Great progress in developing 500 MHz single cell superconducting cavity in China. Sci. China Phys. Mech. Astron. **54** (Suppl 2), 169–173 (2011). doi: 10.1007/s11433-011-4591-7

[4] N. Banerjee, G. Hoffstaetter, M. Liepe et al., Active Suppression of Microphonics Detuning in high QL Cavities. Phys. Rev. Accel. Beams. **22**, 052002 (2019). doi: 10.1103/PhysRevAccelBeams.22.052002

[5] J.Y. Ma, F. Qiu, L.B. Shi et al., Precise calibration of cavity forward and reflected signals using low-level radio-frequency system. Nucl. Sci. Tech. **33**, 4 (2022). doi: 10.1007/s41365-022-00985-4

[6] W. Schappert, Y. Pischalnikov, Recent progress at Fermilab controlling Lorentz force detuning and microphonics in superconducting cavities. Proc. 4th Int. Part. Accel. Conf. (IPAC). (2013).

[7] J.Y. Ma, C.Y. Xu, A.D. Wu et al., Measurement of the cavity-loaded quality factor in superconducting radio-frequency systems with mismatched source impedance. Nucl. Sci. Tech. **34**, 123 (2023). doi: 10.1007/s41365-023-01281-5

[8] X.Y. Pu, H.T. Hou, Y. Wang et al., Frequency sensitivity of the passive third harmonic superconducting cavity for SSRF. Nucl. Sci. Tech. **31**, 31 (2020). doi: 10.1007/s41365-020-0732-x

[9] M. Doleans, S.H. Kim, Insights in the physics of the dynamic detuning in SRF cavities and its active compensation. Conf. Proc. C **030512**, 1599 (2003).

[10] A.D. Wu, S.H. Zhang, W.M. Yue et al., Design study on medium beta superconducting half-wave resonator at IMP. Nucl. Sci. Tech. **27**, 80 (2016). doi: 10.1007/s41365-016-0081-y

[11] W. Cichalewski, J. Sekutowicz, A. Napieralski et al., Continuous wave operation of superconducting accelerating cavities with high loaded quality factor. IEEE Trans. Nucl. Sci. **67**(9), 2119–2127 (2020). doi: 10.1109/TNS.2020.2993539

[12] A. Bellandi, J. Branlard, J. Diaz Cruz et al., Narrow bandwidth active noise control for microphonics rejection in superconducting cavities at LCLS-II. arXiv preprint **2209**, 13896 (2022). doi: 10.48550/arXiv.2209.13896

[13] H.T. Hou, J.F. Chen, Z.Y. Ma et al., Prototypes fabrication of 1.3 GHz superconducting RF components for SHINE. Proc. Int. Conf. RF Superconductivity **2019**, 164-167 (2019). doi: 10.18429/JACoW-SRF2019-MOP049

[14] D. Li, Q. Wang, P. Zhang et al., Active microphonics noise suppression based on DOB control in 166.6-MHz superconducting cavities for HEPS. Radiat. Detect. Technol. Methods **5**, 153–160 (2021). doi: 10.1007/s41605-020-00231-8

[15] F. Qiu, S. Michizono, T. Matsumoto et al., Combined disturbance-observer-based control and iterative learning control design for pulsed superconducting radio frequency cavities. Nucl. Sci. Tech. **32**, 56 (2021). doi: 10.1007/s41365-021-00894-y

[16] G. Jiang, C. Xu, F. Qiu et al., Feedforward control strategies for rapid phase adjustment of superconducting cavities. IEEE Trans. Nucl. Sci. **70**(2), 93-104 (2023). doi: 10.1109/TNS.2023.3237837

[17] J. Vincent, D. Morris, N. Usher et al., On active disturbance rejection based control design for superconducting RF cavities. Nucl. Instrum. Methods Phys. Res., Sect. A **643**(1), 11–16 (2011). doi: 10.1016/j.nima.2011.04.033

[18] Z. Q. Geng, Superconducting cavity control and model identification based on active disturbance rejection control. IEEE Trans. Nucl. Sci. **64**(3), 951-958 (2017). doi: 10.1109/TNS.2017.2663660

[19] F. Qiu, S. Michizono, T. Miura et al., Real-time cavity simulator-based low-level radio-frequency test bench and applications for accelerators. Phys. Rev. Accel. Beams **21**(3), 032003 (2018). doi: 10.1103/PhysRevAccelBeams.21.032003

[20] M. Liu, Z.H. Mi, W.M. Pan et al., Design of 648 MHz superconducting cavity tuner for China Spallation Neutron Source phase II. High Power Laser Part. Beams **35**, 124007 (2023). doi: 10.11884/HPLPB202335.230227

[21] X.Y. Zhang, P. Sha, W.M. Pan et al., The mechanical design, fabrication and tests of dressed 650 MHz 2-cell superconducting cavities for CEPC. Nucl. Instrum. Methods Phys. Res., Sect. A **1031**, 166590 (2022). doi: 10.1016/j.nima.2022.166590

[22] X. Li, H. Sun, C.L. Zhang et al., Design of rapid tuning system for a ferrite-loaded cavity. Radiat. Detect. Technol. Methods **5**, 324-331 (2021). doi: 10.1007/s41605-021-00274-7

[23] P.P. Gong, Y.B. Zhao, H.T. Hou et al., Tuning control system of a third harmonic superconducting cavity in the Shanghai Synchrotron Radiation Facility. Nucl. Sci. Tech. **30**, 157 (2019). doi: 10.1007/s41365-019-0655-4

[24] Y. Zong, J.F. Chen, D. Wang et al., Accelerating gradient improvement in nitrogen-doped superconducting radio-frequency cavities for SHINE. Nucl. Instrum. Methods Phys. Res., Sect. A **1057**, 168724 (2023). doi: 10.1016/j.nima.2023.168724

[25] J.R. Delahaye, Phase and amplitude stabilization of beam-loaded superconducting resonators. Proc. Int. LINAC Conf. **1992**, 16 (1992).

[26] Z.K. Liu, C. Wang, L.H. Chang et al., Modeling the interaction of a heavily beam loaded SRF cavity with its low-level RF feedback loops. Nucl. Instrum. Methods Phys. Res., Sect. A **894**, 57-71 (2018). doi: 10.1016/j.nima.2018.03.046

[27] T. Schilcher, Vector sum control of pulsed accelerating fields in Lorentz force detuned superconducting cavities. PhD Thesis (1998).

[28] R.T. Keshwani, S. Mukhopadhyay, R.D. Gudi et al., Comparative investigations on detuning estimator for experimental RF cavity. IEEE Trans. Instrum. Meas. **72** (2023). doi: 10.1109/TIM.2023.3311075

[29] Z. Gao, Y. He, W. Chang et al., A new microphonics measurement method for superconducting RF cavities. Nucl. Instrum. Methods Phys. Res., Sect. A **767**, 212-217 (2014). doi: 10.1016/j.nima.2014.08.030

[30] S.N. Simrock, Lorentz force compensation of pulsed SRF cavities. Proc. Int. LINAC Conf. **2002** (2002).

[31] T. Li, B. Zhang, L. B. Liu et al., design and test of the helium pneumatic tuner based on 162.5 MHz superconducting cavity. Nucl. Tech. **010**, 1-5 (2015).

[32] C.T. Somefun, S.A. Daramola, T.E. Somefun, Advancements and applications of adaptive filters in signal processing. J. Eng. Sci. Appl. **2024**, 1259-1272 (2024). doi: 10.18280/jesa.570502

[33] X.F. Huang, Y. Sun, G.W. Wang et al., Measurement of the transfer function for a spoke cavity of C-ADS Injector I. Chin. Phys. C **41**(4), 047001 (2017). doi: 10.1088/1674-1137/41/4/047001

[34] A. Neumann, W. Anders, O. Kugeler et al., Analysis and active compensation of microphonics in continuous wave narrow-band superconducting cavities. Phys. Rev. ST Accel. Beams **13**, 082001 (2010).

[35] A. Bellandi, J. Branlard, A. Eichler et al., Integral resonance control in continuous wave superconducting particle accelerators. IFAC-PapersOnLine **53**(2), 361–367 (2020). doi: 10.1016/j.ifacol.2020.12.186